batteries

MDPI

Article

Modeling of a Non-Aqueous Redox Flow Battery for Performance and Capacity Fade Analysis

Mirko D'Adamo [1,2,3], Nicolas Daub [4], Lluis Trilla [2], Jose A. Saez-Zamora [1] and Juan Manuel Paz-Garcia [5,*]

[1] NVISION, Gran Via Carles III, 124, ent. 1a, 08034 Barcelona, Spain; mirko.dadamo@nvision.es (M.D.); jose.saez@nvision.es (J.A.S.-Z.)
[2] Institut de Recerca en Energia de Catalunya—IREC, Jardins de les Dones de Negre 1, 2ª pl., 08930 Sant Adrià del Besòs, Spain; lltrilla@irec.cat
[3] Department of Control, Robotics and Computer Vision, Barcelona School of Industrial Engineering (ETSEIB), Universitat Politècnica de Catalunya (UPC), Diagonal 647, 08034 Barcelona, Spain
[4] Department of Chemical Engineering and Chemistry, Research Group of Molecular Materials and Nanosystems, Institute for Complex Molecular Systems, Eindhoven University of Technology, 5600 MB Eindhoven, The Netherlands; n.daub@tue.nl
[5] Department of Chemical Engineering, University of Malaga, 29071 Malaga, Spain
* Correspondence: juanma.paz@uma.es

Abstract: This study presents a prototype non-aqueous redox flow battery that advances the capabilities of conventional systems by achieving a wide operational voltage range, high efficiency, and prolonged cycle life. Leveraging the redox pair 10-[2-(2-methoxy ethoxy)ethyl]-10H-phenothiazine and 2-ethylterephthalonitrile, the system delivers a discharge cell voltage ranging from approximately 2.25 V to 1.9 V. To address the economic challenges associated with non-aqueous redox flow batteries, this work explores a cost-efficient design using a symmetric cell architecture and a low-cost, porous separator. To evaluate the feasibility and scalability of this approach, a 2D time-transient reactive transport model is developed, integrating Nernst–Planck electroneutrality principles and porous electrode kinetics. The model is optimized and validated against experimental charge/discharge cycles, accurately predicting voltage behavior. Additionally, the study provides crucial insights into the crossover phenomenon, elucidating the transport dynamics and spatial distribution of active species within the cell. This comprehensive framework establishes a robust foundation for future efforts to scale and optimize non-aqueous redox flow batteries for large-scale energy storage applications, bringing them closer to commercial viability.

Keywords: redox flow batteries; multiphysics modeling; crossover diffusion; non-aqueous redox flow battery; capacity fade; operational voltage window; voltage prediction

check for updates

Academic Editor: Dino Tonti

Received: 14 November 2024
Revised: 13 December 2024
Accepted: 20 December 2024
Published: 27 December 2024

Citation: D'Adamo , M.; Daub, N.; Trilla, L.; Saez-Zamora, J.A.; Paz-Garcia, J.M. Modeling of a Non-Aqueous Redox Flow Battery for Performance and Capacity Fade Analysis. *Batteries* **2025**, *11*, 8. https://doi.org/10.3390/batteries11010008

1. Introduction

The global energy landscape is undergoing a significant transformation driven by the need to reduce greenhouse gas emissions and transition to more sustainable energy solutions. Traditional fuels, which have long been the dominant sources of global electricity generation, remain major contributors to carbon emissions and climate change. However, the rapid growth of renewable energy sources—such as solar, wind, and hydropower—is beginning to challenge this conventional energy paradigm. Despite their potential to provide clean energy, renewable resources are inherently intermittent, creating a critical need for efficient energy storage solutions. These solutions are essential to ensure a stable and reliable energy supply during periods of low production.

In this context, redox flow batteries (RFBs) have emerged as one of the most promising technologies for large-scale, long-term energy storage [1]. RFBs offer several advantages, including scalability, flexible design, and the ability to decouple energy storage capacity from power generation. These features make them particularly suitable for integrating renewable energy into the grid, enhancing energy security and supporting the global energy transition [1,2].

The concept of RFBs dates back to the 1980s, with early models primarily focusing on aqueous systems, particularly vanadium-based RFBs (VRFBs) [3–5]. These early developments addressed key challenges related to electrolyte pumping, electrochemical performance, and flow cell design. Over time, more sophisticated models have been developed, incorporating complex phenomena such as temperature effects, the impact of the specific surface area of the electrodes, ion transport, side reactions, and electrolyte degradation [6–8]. Recent advances in RFB technology have focused on enhancing energy density, improving round-trip efficiency, and extending battery lifespan, making RFBs a viable option for future large-scale energy storage applications.

RFBs offer the benefit of independent scaling for capacity and power output. That is, the capacity of an RFB is dependent on the size of the electrolyte storage tanks and power output on the reactor size [9]. This is different from a standard battery, where the capacity is proportional to the size of the electrodes. Therefore, RFBs enable substantial energy storage capacity without the expense of large surface-area electrodes.

In recent years, research has increasingly focused on non-aqueous redox flow batteries (NARFBs), as they can operate in organic solvents that offer wider electrochemical windows, aiming to achieve higher energy densities. In NARFBs, some corrosion problems may be avoided, and some organic solvents may work at temperature ranges different from those of water-based batteries. Furthermore, some organic materials could be cheaper than metals, such as vanadium, making the NARFBs economically advantageous at bigger scales [10–13].

However, despite the potential advantages of NARFBs, several critical challenges remain unresolved. One of the primary obstacles is the reduced solubility of redox-active materials in non-aqueous solvents, which limits the overall energy capacity. Furthermore, non-aqueous systems tend to exhibit higher ionic transport resistance, resulting in lower conductivity and reduced system efficiency. Furthermore, their stability has not reached market maturity yet [14]. Another issue is the lack of suitable membranes. Ion-exchange membranes disable high efficiencies, while porous separators lack selectivity [15]. To overcome these challenges, recent trends in NARFB research have centered on optimizing flow cell design and exploring novel redox-active materials [16,17]. Advances in flow cell engineering—such as improved membrane-separator technology and enhanced electrode configurations—aim to reduce ohmic losses and improve ion transport. At the same time, experimental studies are investigating new active couples, particularly in organic solvents like acetonitrile, which have shown promise for enhancing both energy density and electrolyte stability [18–23].

A promising NARFBs option has emerged through the development of a system combining two simple molecules: 2-ethylterephthalonitrile (ETN) with 10-[2-(2-methoxy ethoxy)ethyl]-10H-phenothiazine (MEEPT) [15,24,25] forming the following redox pair:

$$\mathrm{ETN} + e^- \leftrightarrows \mathrm{ETN}^- \quad ; \quad E^0 = -2.05\ \mathrm{V} \tag{1}$$

$$\mathrm{MEEPT}^+ + e^- \leftrightarrows \mathrm{MEEPT} \quad ; \quad E^0 = 0.31\ \mathrm{V} \tag{2}$$

The mixed flow battery of ETN and MEEPT delivers a cell voltage of 2.36 V (see Figure 1) while also meeting critical criteria such as high stability and efficiency.

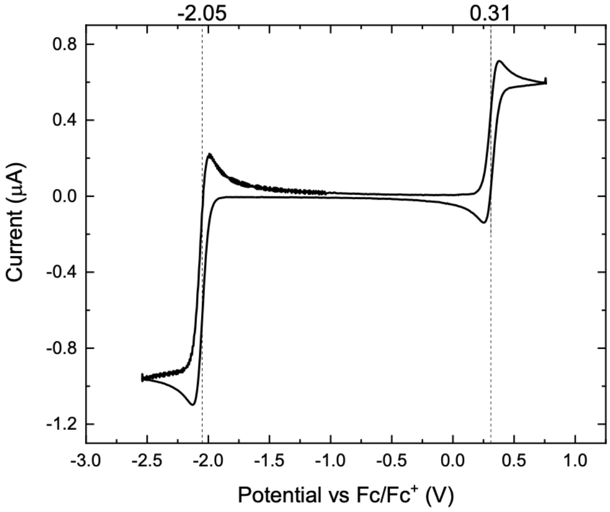

Figure 1. Initial cyclic voltammetry of the battery solution containing 50 mM of ETN and MEEPT in 200 mM TBA-PF6 acetonitrile.

The performance of the proposed cell is promising, retaining almost 90% of the battery capacity after 100 cycles and achieving average energy efficiencies of above 73% (see Supplementary Materials for volumetric discharge capacity and Coulombic, voltaic, and energy efficiencies in 100 cycles, Figure S1, as well as the Nyquist plots before and after 100 cycles, Figure S2). The Nyquist plot shows that, after 100 cycles, there is just a slight increase in the battery's internal resistance, which can be attributed to the crossover effect. Importantly, this cell uses an inexpensive, porous separator, enabling operation at high currents. These experimental results represent a major step in maturing NARFBs and provide a strong foundation for future research into the next generation of scalable, high-performance energy storage technologies.

A comprehensive physicochemical and numerical model was implemented to further improve this system to simulate the electrochemical and transport behavior of a NARFB cell operating with the proposed ETN/MEEPT redox pair. The model incorporates key phenomena such as ion transport, charge conservation, and electrochemical kinetics, providing detailed insight into the cell's operational characteristics. A series of experiments under controlled conditions was conducted to ensure the model's accuracy and reliabilty. These experiments not only validated the model's predictions but also facilitated the optimization of critical parameters, such as the reaction rate constants, enhancing the model's predictive capability. The agreement between the experimental data and simulation results underscores the robustness of the model, making it a valuable tool for understanding cell performance under various operating conditions.

This work represents a significant step toward the practical implementation of NARFB technology and provides a solid foundation for future efforts aimed at scaling up the system for larger applications. By bridging the gap between theoretical modeling and experimental validation, this study contributes to the advancement of energy storage technology, particularly in the design and optimization of next-generation flow batteries.

2. Materials and Methods

The experimental work was performed using a custom-made NARFB cell created at the Eindhoven University of Technology. The cell consists of three parts: a negative electrode, a porous separator, and a positive electrode. Measurements under flow conditions were carried out using a zero-gap flow cell. A combination of a graphite charge-collecting plate and one layer of a non-woven carbon paper electrode with an area of 2.55 cm^2 (Sigracet

29AA) was put on either side of the flow cell. A ±10% compression of the felt was achieved by the use of Gore-tex ePTFF gaskets (see Figure 2). The two halves of the cellwere separated by a Daramic 175 porous separator. The gasket window provided an exposed area of the separator, which was used as the active area of the flow cell.

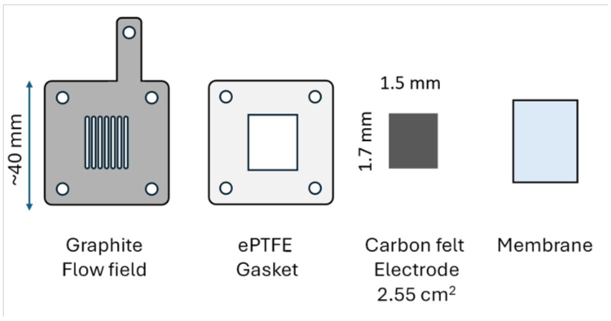

Figure 2. Schematic drawing of the most relevant components of the used cell (only one side).

The catholyte and the anolyte reservoirs were filled with 5 mL of an acetonitrile solution containing 50 mM solution of ETN and MEEPT, as well as 200 mM tetrabutylammonium hexafluorophosphate (TBA-PF_6), which acted as supporting electrolytes. Both reservoirs contained the same initial solution, including the component meant to react in the opposite electrode. This was performed to counterbalance species crossover through the separator and maintain the battery capacity. The cell was connected to the reservoirs by means of peristaltic pumps (Cole-Parmer) by Masterflex C-flex ultra-pump tubing, setting a constant flow rate of 20 mL/min at each electrode. The cell was pretreated by flowing the solution through the cell for 30 min before applying the external electric field. Once the separator was fully wet as evidenced by impedance measurements, the electrochemical cycling was started.

A galvanostatic charge/discharge cycling was performed using currents of ±30 mA/cm^2 for the mixed battery with potential cut-offs at 2.8 V for charging and 1.0 V for discharging. The cycling started with a charging step and lasted for 10 full charge/discharge cycles (approximately 90 min). Figure 3 shows a schematic representation of the continuous redox flow cell.

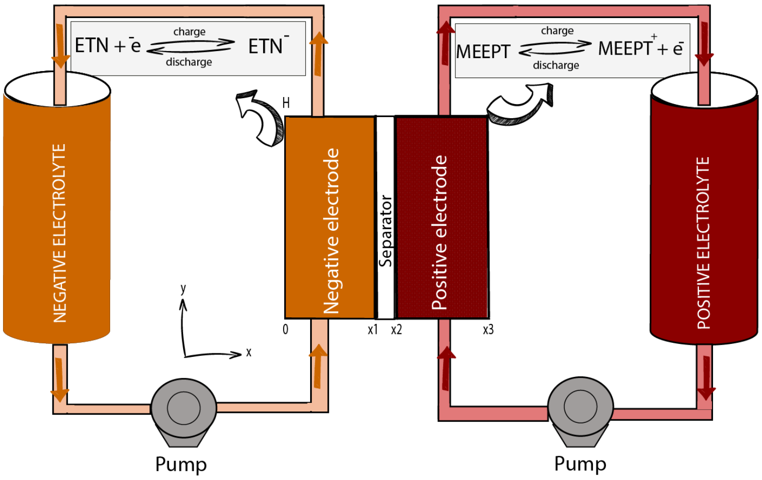

Figure 3. Schematic representation of the continuous redox flow cell.

3. Physicochemical and Numerical Modeling

3.1. The Numerical Model

A Finite Element Method (FEM) model was implemented and used for simulating the coupled reactive transport process [26–29]. The software COMSOL Multiphysics 6.2 was used for the numerical implementation and solution of the model. The model described here can be subdivided into three main parts: (1) the transport of chemical species through the porous media, (2) the heterogeneous electrochemical reactions at the porous electrodes, and (3) the continuous flow of the non-aqueous solutions through the cell and from/to the external reservoirs.

Taking advantage of the rectangular prismatic geometry, the cell was modeled as a 2D domain. The dimension x represents the longitudinal direction, perpendicular to the layers, from the negative to the positive electrode. The dimension y indicates the direction of the flow from the inflow to the outflow sections, assuming that the flow enters the cell in a well-distributed profile. The dimension z is the out-of-plane direction, which is considered homogeneous. Figure 4 represents the schematics of the 2D domain of the cell, showing the inflow and outflow sections, the thickness of the electrodes and separator, and the length of the cell. The figure also illustrates the squared meshes applied to the geometry, consisting of about 3000 elements with a higher density in the separator domain.

To simulate the electrochemical behavior of the cell, the model was subjected to continuous cycles of charge and discharge under a constant galvanostatic current equivalent to the experimental current value. Cut-off voltage values were set between 2.75 V for charging and 1.9 V for discharging, reflecting the experimental observations. Note that the cut-off voltages for the simulation were set based on the experimentally observed results rather than on the experimental method to take into account the possible resolution limitations of the experimental method. A 5 s rest period was included between each half-step to ensure numerical stability and convergence.

The simulation process was divided into two phases. In the first phase, an optimization algorithm was implemented to calibrate the model parameters, minimizing the difference between experimental and simulated results through a least-squares fitting method. Following the optimization, a long-term simulation was conducted for up to 40 charge/discharge cycles to assess model performance. This extended simulation allowed for comparison against the experimental results from 10 cycles and provided insight into the predicted long-term behavior of the cell.

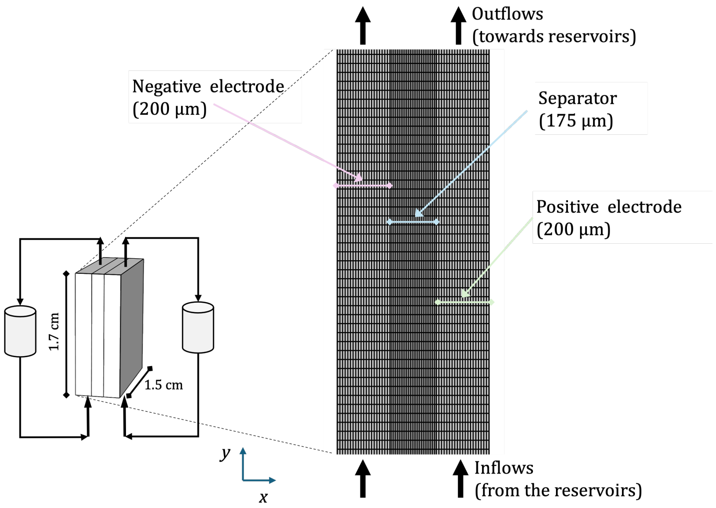

Figure 4. Schematics of the modeled cell. Detail of the 2D domain and the used mesh for the FEM.

3.2. Chemical Species Transport in the Electrodes and Separator

The system of equations that governs the transport of species is based on a set of continuity equations (microscopic mass conservation) for each chemical species, i (with $i = \text{TBA}^+$, PF6^-, ETN, ETN$^-$, MEEPT, MEEPT$^+$), coupled with the electroneutrality condition. The continuity equation for the species i is

$$\frac{\partial \epsilon c_i}{\partial t} + \nabla \vec{J_i} = r_i \tag{3}$$

where ϵ (dimensionless) is the porosity of the medium, c_i (mol/m^3) is the concentration, $\vec{J_i}$ (mol/m^2/s) is the flux term, and r_i (mol/m^3/s) is the source (chemical reaction) term. In the electrode domains, r_i refers to the electrochemical reactions at the electrodes. In the separator domain, r_i is set to zero.

The flux term $\vec{J_i}$ is defined according to the Nernst–Planck equation for chemical species in porous media, accounting for the coupled electro-diffusion transport phenomena and the convective transport as

$$\vec{J_i} = -D_i^{\text{eff}} \nabla c_i - c_i U_i^{\text{eff}} \nabla \phi + \vec{v} c_i \tag{4}$$

where D_i^{eff} (m^2/s) is the effective diffusion coefficient, U_i^{eff} (m^2/s/V) is the effective ionic mobility coefficient, ϕ (V) is the electrolyte potential, and $\vec{v}$ (m/s) is the velocity field that refers to the convection flow of solution in the positive y direction at the electrodes but also to the possible flow in the longitudinal direction between the electrodes for phenomena such as electro-osmosis.

The effective diffusion coefficient D_i^{eff} takes into account the porosity of the porous material ϵ and other aspects such as tortuosity. The Bruggemann correction, widely accepted in porous media formed by homogeneous spherical particles, is used to model the effective transport coefficient using ϵ and a parameter β, defined as the Bruggemann factor:

$$D_i^{\text{eff}} = \epsilon^{\beta} D_i \tag{5}$$

The Bruggemann factors for the electrodes β_{el} and the separator β_{se} were obtained through a parameter optimization method.

According to the dilute solution approximation, the ionic mobility coefficient U_i^{eff} is estimated from the diffusion coefficient by means of the Nernst–Einstein equation:

$$U_i^{\text{eff}} = \frac{F z_i}{RT} D_i^{\text{eff}} \tag{6}$$

where F (C/mol$_\text{e}$) is Faraday's constant, z_i (mol$_\text{e}$/mol) is the ionic charge of the chemical species, R (J/K/mol) is the ideal gas constant, and T (K) is the temperature.

The system of $N = 6$ equations is completed with the electroneutrality condition, which ensures that the sum of the charges of all species at any specific point of space is equal to zero:

$$\sum_{i=1}^{N} z_i c_i = 0 \tag{7}$$

According to this, the system of $N + 1$ equations (N mass balance equations and the electroneutrality condition) fully defines the transport process and allows the calculation of N concentration profiles, c_i, and the electric potential profile ϕ in the electrolyte.

3.3. Electrochemical Reactions

The chemical reactions take place at the interface between the solid particles of the porous electrodes and the electrolyte. The kinetics of the electrode reactions (1) and (2) are described by the Butler–Volmer equation:

$$i_{\mathrm{neg}} = i_{\mathrm{neg},0}a\left(\frac{c_{\mathrm{ETN},s}}{c_{\mathrm{ETN}}}\exp\left(\frac{\alpha_{\mathrm{neg}}F}{RT}\eta_{\mathrm{neg}}\right) - \frac{c_{\mathrm{ETN}^-,s}}{c_{\mathrm{ETN}^-}}\exp\left(-\frac{(1-\alpha_{\mathrm{neg}})F}{RT}\eta_{\mathrm{neg}}\right)\right) \quad (8)$$

for the negative electrode, and

$$i_{\mathrm{pos}} = i_{\mathrm{pos},0}a\left(\frac{c_{\mathrm{MEEPT},s}}{c_{\mathrm{MEEPT}}}\exp\left(\frac{\alpha_{\mathrm{pos}}F}{RT}\eta_{\mathrm{pos}}\right) - \frac{c_{\mathrm{MEEPT}^+,s}}{c_{\mathrm{MEEPT}^+}}\exp\left(-\frac{(1-\alpha_{\mathrm{pos}})F}{RT}\eta_{\mathrm{pos}}\right)\right) \quad (9)$$

for the positive electrode.

In Equations (8) and (9), a ($\mathrm{m}^2/\mathrm{m}^3$) is the specific surface area of the porous electrodes, $i_{\mathrm{neg},0}$ and $i_{\mathrm{pos},0}$ are the reference exchange current densities, $c_{\mathrm{MEEPT},s}$ and $c_{\mathrm{ETN},s}$ are the concentrations of active species on the solid porous electrode, α is the charge transfer coefficient, and η is the overpotential at the electrodes:

$$\eta = (\phi_s - \phi_e) - E^{eq} \quad (10)$$

where $(\phi_s - \phi_e)$ is the difference between the solid- and electrolyte-phase potentials, representing the actual potential in the real cell environment, and E^{eq} (V) is the equilibrium potential, calculated using the Nernst equation:

$$E^{eq} = E^0 - \frac{RT}{nF}\ln\left(\frac{c_{i,red}}{c_{i,ox}}\right) \quad (11)$$

where E^0 ($\approx$ 2.36 V) is the standard reduction potential and n is the number of electrons involved in the reaction.

3.4. Coupling with the External Reservoirs

Each electrode of the cell has an inflow and an outflow system, pumping the non-aqueous solution from and towards separated containers that act as reservoirs. As the concentration of the reactants in the reservoir changes, the battery charges or discharges. As mentioned before, the capacity of the RFB is directly related to the volume and concentration of these external reservoirs. In the model presented here, the reservoirs are modeled as perfectly mixed tanks, described through corresponding mass balance equations:

$$V_j\frac{\partial c_{i,j}}{\partial t} = \int_{\partial\Omega_{in,j}} c_{i,j}^{in}(\vec{n}\cdot\vec{v}) - c_{i,j}Q \quad (12)$$

where j = (neg or pos) refers to the negative or the positive electrodes, V_j (m^3) is the volume of the reservoir and $\vec{v}$ (m/s) is the velocity vector. The integral form was used, as the velocity profile within the electrode may differ in the longitudinal x direction.

3.5. Model Parameters

In order to obtain the results presented in this section, a set of known parameters was used in the model. Known parameters refer to the cell geometry, the flow and electrical operation conditions, the chemical properties of the involved chemical species and materials, and the initial concentrations. These parameters are described in Tables 1 and 2.

In addition to the known parameters, a set of fixing parameters was used in the model. The fitting parameters in the presented model were those describing the chemical kinetics for both electrode reactions and the Bruggemann factor for the separator. An optimization method was used to search for the most suitable value of these fitting parameters, aiming to achieve the best match between the simulated and the experimental cell value. Table 3 lists the values of the estimated parameters that resulted in the simulations presented in this section, with the best fitting being between the experiments and the simulations.

Table 1. Geometrical and operational parameters.

Parameter	Value	Units	Description
a	1.1×10^7	[m^2/m^3]	Specific surface area
ϵ_s	0.57	[dimensionless]	Porosity of the separator
ϵ	0.88	[dimensionless]	Porosity of the porous electrodes
H	1.7	[cm]	Height of the cell
L_e	1.5	[cm]	Length of the cell
W_e	190	[µm]	Thickness of the electrodes
W_s	175	[µm]	Thickness of the separator
Q	20	[mL/min]	Flow rate circulated through each electrode
V	5	[mL]	Volume of circulated solution in each electrode
i_{app}	30	[mA/cm^2]	Applied current density

Table 2. Diffusion coefficients and initial concentrations.

Parameter	Value	Units	Parameter	Value	Units
D_{TBA^+}	0.519×10^{-9}	[m²/s]	$c_{\mathrm{TBA}^+,0}$	200	[mM]
D_{PF6^-}	1.515×10^{-9}	[m²/s]	$c_{\mathrm{PF6}^-,0}$	200	[mM]
D_{ETN}	2.81×10^{-9}	[m²/s]	$c_{\mathrm{ETN},0}$	50	[mM]
D_{ETN^-}	3.288×10^{-9}	[m²/s]	$c_{\mathrm{ETN}^-,0}$	0	[mM]
D_{MEEPT}	1.95×10^{-9}	[m²/s]	$c_{\mathrm{MEEPT},0}$	50	[mM]
D_{MEEPT^+}	3.4×10^{-9}	[m²/s]	$c_{\mathrm{MEEPT}^+,0}$	0	[mM]

Table 3. Estimated parameters.

Parameter	Value	Units	Description
β_{el}	1.31	[unitless]	Bruggemann factor of the electrodes
β_{se}	1.55	[unitless]	Bruggemann factor of the separator
α_{neg}	0.509	[unitless]	Anodic charge transfer coefficient negative electrode
α_{pos}	0.548	[unitless]	Anodic charge transfer coefficient positive electrode
$i_{\mathrm{neg},0}$	3.19	[A/m^2]	Reference exchange current density negative electrode
$i_{\mathrm{pos},0}$	3.61	[A/m^2]	Reference exchange current density positive electrode

The optimization method resulted in very similar values of the Butler–Volmer equation for both electrodes, which is consistent with the fact that both electrodes are identical in terms of materials and fabricating method. The term $i_{j,0}a$ represents the product of the reference exchange current density and the specific surface area of the electrodes.

4. Results and Discussions

4.1. Simulated Voltage and Tank Concentrations

Figure 5a depicts the cell voltage measured in the set of ten consecutive and uninterrupted experimental cycles of charge and discharge, together with the simulated results. Figure 5b shows the simulated cell voltage in cycles 39 and 40. It can be observed that the tested cell maintains cyclability in subsequent cycles (at least in the first ten cycles), and the simulated cell voltage matches fairly well with the experimental results. It can also be observed that between the fifth and the ninth cycles, there is a slight phase difference between the simulated and experimental cycles. However, the gap seems to be due to small fluctuations in the experimentally obtained results, as the simulated results are stable, while the experimental results cycles slightly vary in their period. The fluctuations may be due to small temperature or flow rate differences during the experimental work. Despite this slight phase displacement, the presented model can satisfactorily predict the cell behavior.

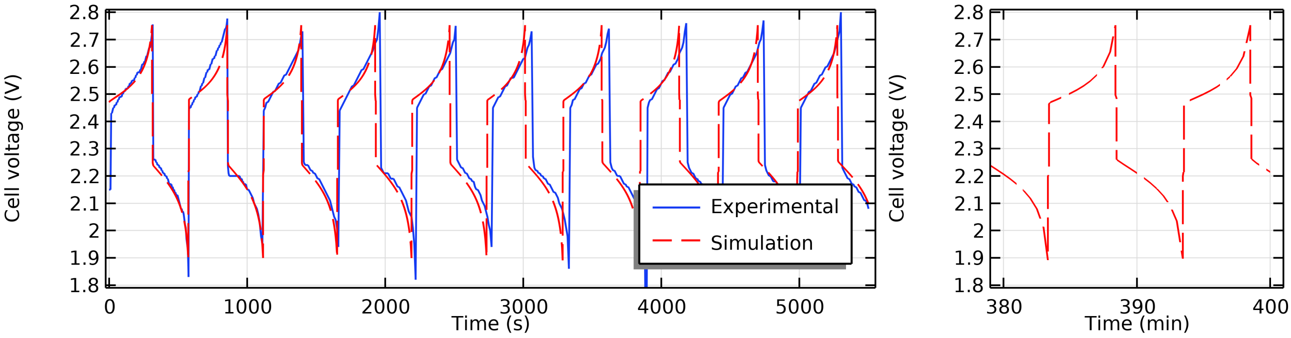

(**a**) First ten cycles (**b**) Cycles number 39 and 40

Figure 5. Simulated and experimental cell voltage during 40 cycles of charge and discharge.

The discharge cycle offers a cell voltage from ≈2.25 V at the start of the discharge down to the cut-off voltage. The charging step occurs between ≈2.45 V and the cut-off voltage. Taking into account the value for the standard redox potential of the redox pair ($E^0 \approx 2.36$ V), the presented model is capable of adequately measuring the overpotential due to variations in the Nernst–Planck equation and the effect of the changing ion concentration. Potential electrochemical impedance spectroscopy was performed before starting the cycling and after 100 cycles of operation (Figure S2). Thereby, the ASR increased by about 7%.

4.2. Active Species Concentrations Distribution Across the Cell

Figures 6 and 7 show, respectively, the concentration in the reservoirs connected to the negative and positive electrodes obtained in the simulations during the first 10 cycles and after 40 cycles. It should be noted that the concentration in the reservoirs is approximately the concentration within the electrodes.

In Figure 6, it can be observed how the concentration of ETN and ETN$^-$ changes during the charge and the discharge steps of the cycles. At the negative electrode, ETN is reduced to ETN$^-$ during the charge, and the opposite reaction occurs during the discharge. Similarly, Figure 7 shows that the concentration of MEEPT and MEEPT$^+$ adjusts to the charge/discharge cycle. During the charge, MEEPT is oxidized to MEEPT$^+$, and the opposite reaction occurs during the discharge.

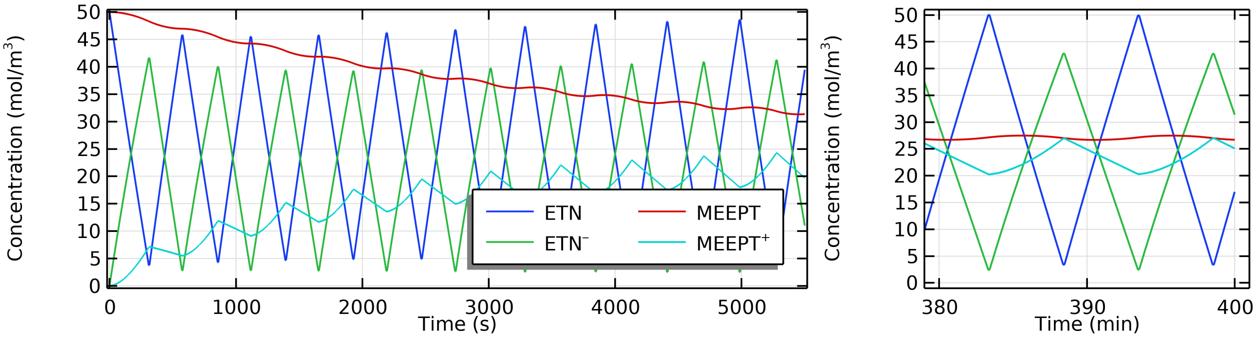

(**a**) First ten cycles (**b**) Cycles number 39 and 40

Figure 6. Simulated concentration in the reservoirs connected to the negative electrode.

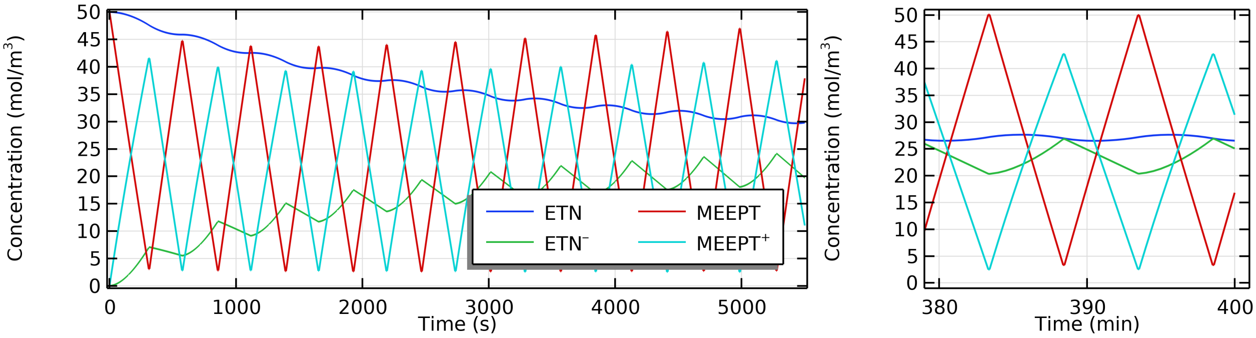

(**a**) First ten cycles

(**b**) Cycles number 39 and 40

Figure 7. Simulated concentration in the reservoirs connected to the positive electrode.

In addition to the electrochemical reactions, electro-diffusion of the chemical species through the separator was also observed, denoted as crossover transport. It should be noted that the initial concentration of the solutions was 50 mM of MEEPT and ETN in both electrodes. Figures 6b and 7b show that after a certain number of cycles, the concentration of MEEPT and MEEPT$^+$ at the negative electrode and ETN and ETN$^-$ at the positive electrode reached a certain stable value. The ionic species MEEPT$^+$ and ETN$^-$, were submitted to oscillations due to the polarization of the electrodes.

The reason to include some initial concentration of the chemical species from the opposite electrode was to hinder the diffusion of active material from each electrode to the opposite one through the semi-permeable separator. The simulation results how stable cyclability and no capacity faded after approximately 40 cycles. In fact, the simulation results show that during the very first cycles, there was a slight decrease in the cell capacity, as the concentration of ETN at the negative electrode and MEEPT at the positive electrodes after the discharge step did not reach the initial value of 50 mM. However, as the cycles proceeded, the cell stabilized, and the concentration of those active species reached the expected 50 mM value associated with the established initial capacity. The stabilization matches with the electro-diffusion of the crossover species. Therefore, it can be concluded that the initial concentration of the active component in the opposite electrode resulted in a compensation of the crossover transport, maintaining the capacity of the battery.

Figure 8 shows the simulated concentration in the reservoirs of the salt components, TBA$^+$ and PF6$^-$ during the first ten cycles. As can be seen, the concentration of salts varies. As the redox reactions and the effect of the electric field applied to the cell promote the migration of the ions, the supporting electrolyte concentration in the different compartments ensures the electroneutrality condition defined in Equation (6). It can be observed that the oscillation of the salts converges to a stable amplitude as the concentration of the ions ETN$^-$ and MEEPT$^+$ balances in the reservoirs with continuous cycling.

Figure 9 shows the concentration of ETN, ETN$^-$, MEEPT, and MEEPT$^+$ in the cell at three specific times, namely, 1150, 1250, and 1350 s, that corresponds with the three chosen positions in the charging step of the third cycle (one at the beginning of the charging step, another halfway, and the last almost reaching the full-charged point). This cycle and position were chosen arbitrarily to show the concentration of the active species in the different parts of the 2D domain of the cell. In each case, the three attached rectangles represent the negative electrode, separator, and positive electrode as explained in Figure 4.

In Figure 9, it can be seen that the concentration of the different components in the electrode domains is approximately constant with respect to the position, showing only significant concentration gradients in the separator region. This indicates that the cell behavior is controlled by the kinetics equation rather than by the transport of chemical species. Supporting the results previously discussed, it can be seen that the chemical species are transported through the separator.

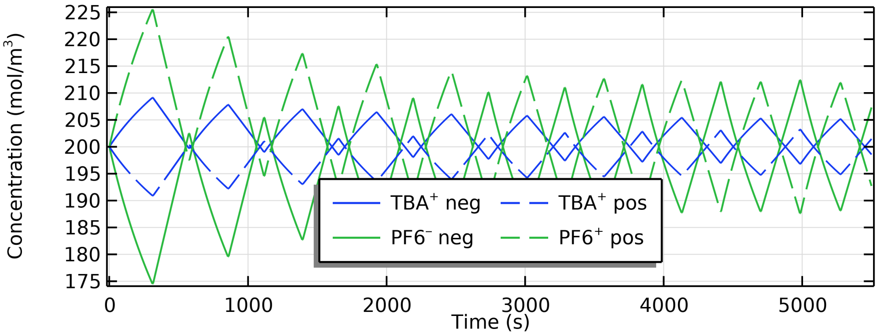

Figure 8. Simulated concentration of the salt in the reservoirs connected to the electrodes during the first cycle.

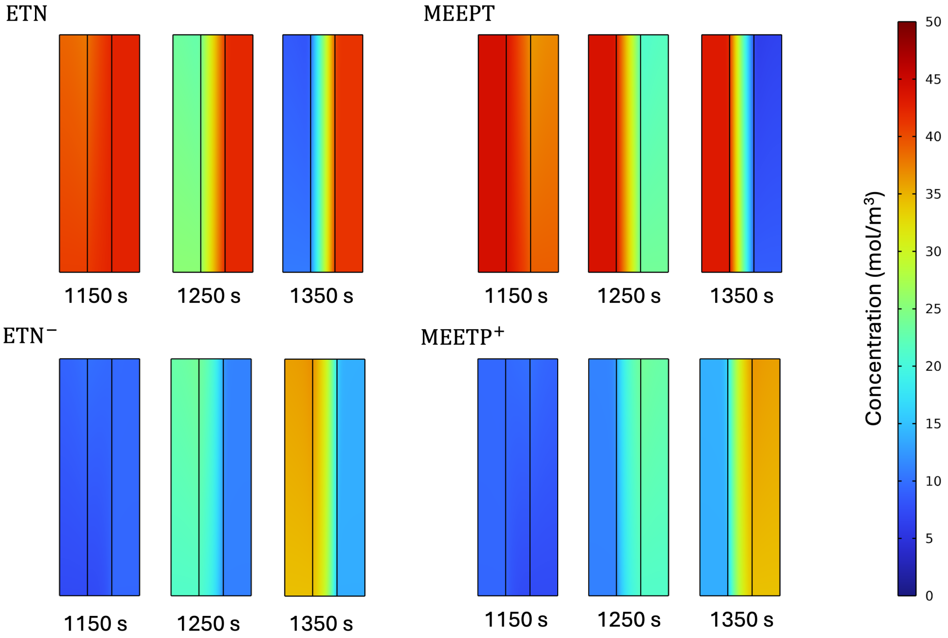

Figure 9. Simulated concentration in the reservoirs connected to the electrodes during the third cycle.

5. Conclusions

The NARFB prototype presented in this study achieved stable cycling over 100 cycles with energy efficiencies above 73%. These results underscore the durability and robust performance of the battery. Through this integrated experimental and theoretical approach, a more comprehensive understanding of the operating characteristics of the battery has been achieved. These findings pave the way for the resolution of challenges, such as the deterioration of long-term capacity and the chemical degradation of active components, essential for real-world deployment.

The 2D multiphysics model developed in this work accurately predicted the behavior of the cell potential, demonstrating its effectiveness in advancing the design of the NARFB prototype. This model serves as a critical tool for optimizing key cell parameters, such as current density, flow rate, and electrolyte composition, which are crucial to improving both battery efficiency and scalability. Although the model has shown strong predictive capability, future work will address its limitations by extending the geometry to 3D, investigating competitive electrochemical reactions, and incorporating degradation mechanisms to simulate capacity fade over extended cycles. Such advancements will further refine the accuracy and applicability of the model for high-performance, large-scale NARFB systems.

Supplementary Materials: The following supporting information can be downloaded at: https://www.mdpi.com/article/10.3390/batteries11010008/s1, Figure S1: Volumetric discharge capacity, coulombic, voltaic and energy efficiencies versus cycle number in 100 cycles; Figure S2: Potential electrochemical impedance spectroscopy before and after 100 cycles.

Author Contributions: Conceptualization, N.D., M.D. and J.M.P.-G.; methodology, M.D. and J.M.P.-G.; investigation, M.D., N.D., J.M.P.-G., L.T. and J.A.S.-Z.; writing—original draft preparation, M.D. and J.M.P.-G.; writing—review and editing, N.D., M.D. and J.M.P.-G.; flow cell experiments, N.D.; visualization, M.D.; supervision, J.M.P.-G.; project administration, M.D. and L.T. All authors have read and agreed to the published version of the manuscript.

Funding: This study has been financed by the support of Pla de Doctorats Industrials de la Secretaria d'Universitats i Recerca del Departament d'Empresa i Coneixement de la Generalitat de Catalunya (https://doctoratsindustrials.gencat.cat). The research received funding from the Dutch Research Council (NWO) via a Spinoza award. The authors acknowledge the grant from the TED2021-130756B-C31 funded by the MCIN/AEI/10.13039/501100011033.

Data Availability Statement: The original contributions presented in the study are included in the article and supplementary materials, further inquiries can be directed to the corresponding author.

Acknowledgments: The authors gratefully acknowledge the technical and academic support of the Multiphysics Modeling School of the University of Malaga (Spain) (https://www.multiphysics.uma.es).

Conflicts of Interest: Authors Mirko D'Adamo and Jose A. Saez-Zamora were employed by the company NVISION. Eindhoven University of Technology has filed a patent application based on the results described in this paper.

References

1. Sanchez-Diez, E.; Ventosa, E.; Guarnieri, M.; Trovò, A.; Flox, C.; Marcilla, R.; Soavi, F.; Mazúr, P.; Aranzabe, E.; Ferret, R. Redox flow batteries: Status and perspective towards sustainable stationary energy storage. *J. Power Sources* **2021**, *481*, 228804. [CrossRef]
2. Kortekaas, L.; Fricke, S.; Korshunov, A.; Cekic-Laskovic, I.; Winter, M.; Grünebaum, M. Building Bridges: Unifying Design and Development Aspects for Advancing Non-Aqueous Redox-Flow Batteries. *Batteries* **2023**, *9*, 4. [CrossRef]
3. Shah, A.A.; Watt-Smith, M.J.; Walsh, F.C. A dynamic performance model for redox-flow batteries involving soluble species *Electrochim. Acta* **2008**, *53*, 8087.
4. Al-Fetlawi, H.; Shah, A.A.; Walsh, F.C. Non-isothermal modelling of the all-vanadium redox flow battery *Electrochim. Acta* **2009**, *55*, 78–89.
5. Al-Fetlawi, H.; Shah, A.A.; Walsh, F.C. Dynamic modelling of hydrogen evolution effects in the all-vanadium redox flow battery *Electrochim. Acta* **2010**, *55*, 1125–1139.
6. Knehr, K.W.; Kumbur, E.C. Open circuit voltage of vanadium redox flow batteries: Discrepancy between models and experiments. *Electrochem. Commun.* **2011**, *13*, 342. [CrossRef]
7. Modak, S.V.; Shen, W.; Singh, S.; Herrera, D.; Oudeif, F.; Goldsmith, B.R.; Huan, X.; Kwabi, D.G. Understanding capacity fade in organic redox-flow batteries by combining spectroscopy with statistical inference techniques. *Nat. Commun.* **2023**, *14*, 3602. [CrossRef]
8. Briot, L.; Petit, M.; Cacciuttolo, Q.; Péra, M.-C. Aging phenomena and their modelling in aqueous organic redox flow batteries: A review. *Power Sources* **2022**, *536*, 231427. [CrossRef]
9. Leung, P.; Li, X.; de León, C.P.; Berlouis, L.; Lowa, T.J.; Walsha, F.C. Progress in redox flow batteries, remaining challenges and their applications in energy storage. *RSC Adv.* **2012** *2*, 10125–10156. [CrossRef]
10. Milshtein, J.D.; Barton, J.L.; Darling, R.M.; Brushett, F.R. 4-acetamido-2,2,6,6-tetramethylpiperidine-1-oxyl as a model organic redox active compound for nonaqueous flow batteries *J. Power Sources* **2016**, *327*, 151. [CrossRef]
11. Vagin, M.; Che, C.; Gueskine, V.; Berggren, M.; Crispin, X. Ion-Selective Electrocatalysis on Conducting Polymer Electrodes: Improving the Performance of Redox Flow Batteries *Adv. Funct. Mater.* **2020**, *30*, 2007009. [CrossRef]
12. Kocyigit, N.; Gencten, M.; Sahin, M.; Sahin, Y. A novel vanadium/cobalt redox couple in aqueous acidic solution for redox flow batteries. *Int. J. Energy Res.* **2020**, *44*, 411. [CrossRef]

13. Qian, X.; Chang, D.R.; Jung, S. Experimental and computational study on alloxazine derivative based organic redox flow battery *Chem. Eng. J.* **2022**, *429*, 2007009.
14. Milshtein, J.D.; Barton, J.L.; Carney, T.J.; Kowalski, J.A.; Darling, R.M.; Brushett, F.R. Towards Low Resistance Nonaqueous Redox Flow Batteries *J. Electrochem. Soc.* **2017**, *164*, A2487. [CrossRef]
15. Liang, Z.; Attanayake, N.H.; Greco, K.V.; Neyhouse, B.J.; Barton, J.L.; Kaur, A.P.; Eubanks, W.L.; Brushett, F.R.; Susan, A.; Odom, S.A. Comparison of Separators vs Membranes in Nonaqueous Redox Flow Battery Electrolytes Containing Small Molecule Active Materials. *ACS Appl. Energy Mater.* **2021**, *4*, 5443–5451. [CrossRef]
16. Huang, H.; Howl, R.; Agar, E.; Nourani, M.; Golden, J.A.; Cappillino, P. Bioinspired, high-stability, nonaqueous redox flow battery electrolytes *J. Mater. Chem.* **2017**, *5*, 11586. [CrossRef]
17. Zhang, W.; Walser-Kuntz, R.; Tracy, J.S.; Schramm, T.K.; Shee, J.; Head-Gordon, M.; Chen, G.; Helms, B.A.; Sanford, M.S.; Toste, F.D. Indolo[2,3-b]quinoxaline as a Low Reduction Potential and High Stability Anolyte Scaffold for Nonaqueous Redox Flow Batteries. *J. Am. Chem. Soc.* **2023**, *145*, 18877–18887. [CrossRef]
18. Gokoglan, T.C.; Pahari, S.K.; Hamel, A.; Howl, R.; Cappilino, P.J.; Agar, E. Operando spectroelectrochemical characterization of a highly stable bioinspired redox flow battery active material. *J. Electrochem. Soc.* **2019**, *166*, A1745–A1751. [CrossRef]
19. Pahari, S.K.; Gokoglan, T.C.; Visayas, B.R.B.; Woehl, J.; Golen, J.A.; Howland, R.; Mayes, M.L.; Agar, E.; Cappillino, P.J. Designing high energy density flow batteries by tuning active-material thermodynamics. *RSC Adv.* **2021**, *11*, 5432–5443. [CrossRef]
20. Visayas, B.R.B.; Pahari, S.K.; Gokoglan, T.C.; Golen, J.A.; Agar, E.; Cappillino, P.J.; Mayes, M.L. Computational and experimental investigation of the effect of cation structure on the solubility of anionic flow battery active-materials. *Chem. Sci.* **2021**, *12*, 15892. [CrossRef]
21. Hendriks, K.H.; Sevov, C.S.; Cook, M.E.; Sanford, M.S. Multielectron Cycling of a Low-Potential Anolyte in Alkali Metal Electrolytes for Non-aqueous Redox Flow Batteries. *Acs Energy Lett.* **2017**, *2*, 2430–2435. [CrossRef]
22. Daub, N.; Janssen, R.A.J.; Hendriks, K.H. Imide-Based Multielectron Anolytes as High-Performance Materials in Nonaqueous Redox Flow Batteries. *ACS Appl. Energy Mater.* **2021**, *4*, 9248–9257. [CrossRef]
23. Mansha, M.; Anam, A.; Khan, S.A.; Alzahrani, A.S.; Khan, M.; Ahmad, A.; Arshad, M.; Ali, S. Recent Developments on Electroactive Organic Electrolytes for Non-Aqueous Redox Flow Batteries: Current Status, Challenges, and Prospects. *Chem. Rec.* **2024**, *24*, e202300233. [CrossRef]
24. Milshtein, J.D.; Kaur, A.P.; Casselman, M.D.; Kowalski, J.A.; Modekrutti, S.; Zhang, P.L.; Harsha, A.N.; Elliott, C.F.; Parkin, S.R.; Risko, C.; et al. High current density, long duration cycling of soluble organic active species for non-aqueous redox flow batteries. *Energy Environ. Sci.* **2016**, *9*, 3531–3543. [CrossRef]
25. Quinn, A.H.; Ripley, K.P.; Matteucci, N.J.; Neyhouse, B.J.; Brown, C.A.O.; Woltmann, W.P.; Brushett, F.R. Elucidating the Effects of Temperature on Nonaqueous Redox Flow Cell Cycling Performance. *J. Electrochem. Soc.* **2023**, *17*, 120520. [CrossRef]
26. Huang, S.; Lu, Y. Numerical Parametric Investigation of Nonaqueous Vanadium Redox Flow Batteries. *Batteries* **2022**, *8*, 75. [CrossRef]
27. Masi, M.; Paz-Garcia, J.M.; Gomez-Lahoz, C.; Villen-Guzman, M.; Ceccarini, A.; Iannelli, R. Modeling of electrokinetic remediation combining local chemical equilibrium and chemical reaction kinetics *J. Hazard. Mater.* **2019**, *371*, 728–733. [CrossRef]
28. Paz-Garcia, J.M.; Villen-Guzman, M.; Garcia-Rubio, A.; Hall, S.; Ristinmaa, M.; Gomez-Lahoz, C. A coupled reactive-transport model for electrokinetic remediation. In *Electrokinetics Across Disciplines and Continents: New Strategies for Sustainable Development*; Ribeiro, A.B., Mateus, E.P., Couto, N., Eds.; Springer: Cham, Switzerland, 2015; pp. 251–278.
29. Zhou, H.; Zhang, R.; Ma, Q.; Li, Z.; Su, H.; Lu, P.; Yang, W.; Xu, Q. Modeling and Simulation of Non-Aqueous Redox Flow Batteries: A Mini-Review. *Batteries* **2023**, *9*, 215. [CrossRef]